

+SSLIP: Automated Radon-assisted and Rotation-corrected identification of complex HCP slip system activity fields from DIC data

T. Vermeij^{a,b,1}, G. Slokker^{a,1}, C.J.A. Mornout^a, D. König^a, J.P.M. Hoefnagels^{*a}

^a*Dept. of Mechanical Engineering, Eindhoven University of Technology, 5600MB Eindhoven, The Netherlands*

^b*Laboratory for Mechanics of Materials and Nanostructures, Swiss Federal Laboratories for Materials Science and Technology (EMPA), Feuerwerkerstrasse 39, 3602 Thun, Switzerland*

Abstract

Identification of crystallographic slip in metals and alloys is crucial to understand and improve their mechanical behavior. Recently, a novel slip system identification framework, termed SSLIP (for Slip System-based Local Identification of Plasticity), was introduced to leap from conventional trace-based identification to automated, point-by-point identification that exploits the full deformation kinematics. Using microstructure-correlated deformation data (i.e. sub-micron-scale DIC aligned to EBSD), SSLIP matches the measured in-plane displacement gradient tensor to the kinematics of the optimal combination of multiple slip system activities, at each DIC datapoint. SSLIP was applied and demonstrated to be successful on virtual and experimental case studies of FCC and BCC metals. However, for more advanced and anisotropic HCP crystal structures the complete identification of all slip systems was found to be more challenging, posing limitations on automation and flexibility. Here, we propose a significant extension to the SSLIP framework with the aim of automated slip system identification for complex HCP experiments. The main extensions of the SSLIP method, hereinafter referred to as the +SSLIP method, include (i) a pre-selection of slip systems using a Radon transform, (ii) robustness to measured rigid body rotation by simultaneous identification of the local elastic rotation field, (iii) identification of the two best matching slip systems for each data point, and (iv) a procedure to deal with slip systems with in-plane displacement gradient tensors that cannot be discriminated, yielding the full (HCP) slip system activity maps with all slip systems for each grain. The resulting objective identification method does not rely on, e.g., the Schmid factor to select which slip system is active at each point. We show how slip systems from multiple slip families are successfully identified on virtual and real experiments on a Zn polycrystalline coating. We also provide the full Matlab code for +SSLIP on Github.

Keywords: slip system identification, crystallographic slip, SSLIP, HCP plasticity, SEM-DIC, Zinc

1. Introduction

Understanding the mechanisms of plastic deformation in metals and alloys, governed predominantly by crystallographic slip, is fundamental to advancing material science and engineering. Crystallographic slip, the movement of dislocations across slip planes in specific directions, is intrinsic to the material's crystal structure and its response to external stresses. The intricacies of this process are encapsulated in various slip systems, dictating the mechanical properties and behavior of materials under load. However, accurately identifying and quantifying slip system activities poses significant fundamental challenges, that are exacerbated by various dislocation mechanisms, such as the complex interplay of multiple slip systems and the presence of diffuse or intersecting slips, as well as the limitations of existing characterization techniques [1–6].

Over the years, various slip system identification methods have been proposed and applied. Through Scanning Electron Microscopy (SEM), discrete and straight slip bands can be observed and matched to theoretical slip plane traces, based on a measured crystal orientation [7–10]. Additionally, strain maps acquired through SEM-based Digital Image Correlation (SEM-DIC) can be employed for slip trace analysis [11–14]. However, in order to obtain a more complete identification, the slip direction also needs to be considered. Therefore, approaches such as the "Relative Displacement Ratio" (RDR) method [15] and the "Heaviside DIC method" [16] aim to also extract the slip direction from the SEM-DIC displacement field. The Heaviside DIC method incorporates an additional step function within a DIC subset to deduce the slip trace and direction assuming that the slip is confined to a single slip plane resulting in a clean slip step [16]. On the other hand, the RDR method analyzes regular DIC data by comparing displacement component ratios across a distinct slip trace to theoretical Burgers vector ratios [15]. While these methods have proven effective in various studies [17–21], their application is mostly limited to scenarios with well-defined slip traces, struggling with diffuse or complex slip, partly pertaining due to the resolution constraints of SEM-DIC.

To address the complexities in slip system identification and the limitations of current methodologies, Vermeij *et al.* recently introduced an automated identification approach, termed as SSLIP (Slip Systems based Identification of Local Plasticity) [22]. This method leverages the detailed deformation data produced through DIC to facilitate a point-by-point identification of slip system activities across a sample surface. By

*Corresponding author

Email address: j.p.m.hoefnagels@tue.nl (J.P.M. Hoefnagels*)

¹These authors contributed equally.

solving an optimization problem at every SEM-DIC data point, SSLIP matches the measured in-plane kinematics - represented by displacement gradient fields - to a combination of theoretical slip system kinematics derived from Electron Backscatter Diffraction (EBSD) data, after data alignment [4]. This novel approach not only enables the generation of slip system activity fields for each potential slip system but also uncovers the local variations in slip activity, particularly near grain and phase boundaries. Such detailed analysis holds significant promise for enhancing the understanding of plastic deformation mechanisms and allows for more precise comparisons between experiments and theoretical simulations [5, 6, 23, 24], as evidenced by the rapid adoption of the SSLIP method by the research community [25–28].

However, as discussed by Vermeij *et al.* [22], the automated and complete application of SSLIP on hexagonal close-packed (HCP) materials is challenging, due to its high anisotropy and wide range of slip families, resulting in a large number of slip systems with (very) similar in-plane kinematics making them linearly dependent in the optimization problem [22]. By analyzing virtual HCP experiments [22], it was found that in such demanding cases, a preselection of slip systems to limit the number of possibly active slip systems was necessary. While it was demonstrated that manual preselection of slip systems works for the virtual HCP experiment (without elastic rotations) [22] and for single and bicrystal Zn experiments [29], automation is warranted in order to sustain statistical investigations of slip activities in multiple grains. The problem is made worse by elastic rotations, which are not included in the SSLIP optimization framework. Even though the apparent deformations due to elastic rotations are tiny, their effect in the presence of a large number of similar slip systems can often be large. As a result, a convincing, robust experimental demonstration of SSLIP on HCP is lacking, especially a demonstration of many HCP grains for which automatic identification is crucial.

Here we propose extend the current SSLIP method to make it a robust automatic slip identification method for HCP (and other complex) crystals. Therefore, we first propose to implement an automate preselection step by means of a Radon transform [30], known for its ability to detect straight features, i.e. slip bands from strain maps [13], and we will demonstrate the efficiency of this automated preselection step in the presence of complex and diffuse slip. Subsequently, from the preselected slip systems, the best-fitting combination of two of the preselected systems will be identified for each individual data point separately, such that all of the preselected systems can be active throughout the complete crystal. This step employs an optimization algorithm that not only seeks the optimal match based on local kinematics but also incorporates a correction for any additional local rotation. This rotation correction is crucial as it accounts for misalignments and grain rotations, that would otherwise impede accurate slip system

identification, as explained above. By only allowing two slip systems per point, our approach enhances the robustness of the identification process, while avoiding problems in the iterative solution method due to multiple linear-dependent slip systems. We term this extended methodology as +SSLIP – for Radon-assisted, Rotation-corrected, Slip System based Local Identification of Plasticity – to distinguish it from the original SSLIP method.

The significant advancements made with +SSLIP can be most clearly seen from the challenging virtual HCP experiment initially presented in the original SSLIP paper (Section 7 in [22]). Figure 1(a) displays the strain field of this synthetic experiment, where four slip systems are active from four different slip families. The results from the original full SSLIP identification, shown in Figure 1(b), clearly show that several slip systems were misidentified, as marked by the red crosses. In contrast, Figure 1(c) gives a preview of the results of the new +SSLIP approach, utilizing the Radon transform for automated preselection, showing a nearly perfect identification of all four slip systems, as discussed below.

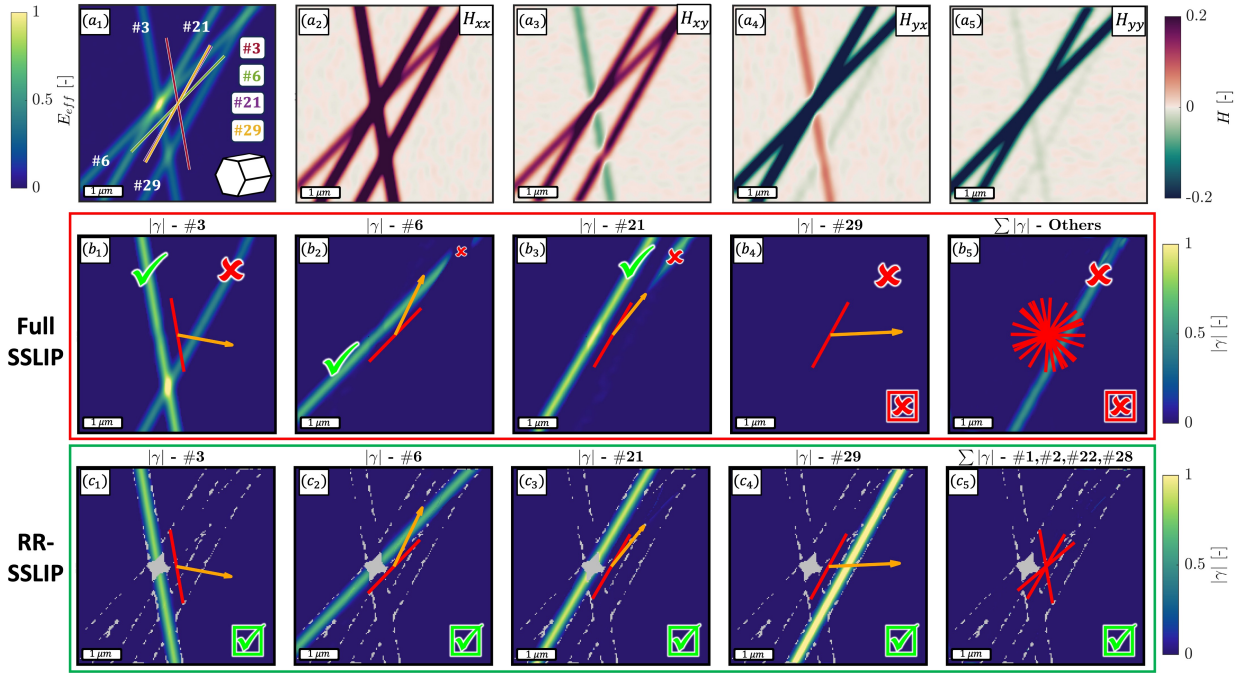


Figure 1: Virtual HCP SEM-DIC experiment, with (a₁) corresponding artificially generated effective strain field, E_{eff} , with strain bands marked and corresponding slip traces of the four included slip systems from different slip families, (a₂)-(a₅) the four in-plane displacement gradient tensor components, respectively H_{xx}^{exp} , H_{xy}^{exp} , H_{yx}^{exp} , H_{yy}^{exp} . (b) The identified slip activity fields using the original SSLIP method, reproduced from [22], with (b₅) showing the sum of all others slip activities that are not supposed to be active. (c) Identification result of the new +SSLIP approach. Green checkmarks indicate correctly identified slip systems, red crosses indicate erroneous ones.

The paper is structured as follows. In Section 2, the +SSLIP method is outlined in detail and demonstrated on the challenging virtual experiment that is introduced in Figure 1. Next, in Section 3 an experi-

mental SEM-DIC case study on HCP is used to demonstrate the power of the +SSLIP method, for selected HCP grains that show various complicated slip mechanisms, showing a robust identification of slip activity fields while considering no less than 30 slip systems from 5 different slip families. Finally, conclusions are summarized in Section 4.

2. Methodology

In this section, we outline the computational framework developed to extend the SSLIP methodology to +SSLIP, mainly for the identification of slip system activities within HCP materials. First, the virtual experiment and the original SSLIP method [22] are recapped, after which the new +SSLIP method is introduced.

2.1. Virtual Experiment and Recapitulation of the original SSLIP Method

The virtual experiment, originally designed as the ultimate challenge for the SSLIP methodology [22], incorporates four overlapping slip systems from different slip families that represent the possible complexity of slip activity in an HCP material. The displacement field \vec{u} is generated using the following slip systems: Basal-3 (#3), PrismI-3 (#6), PyrICA-9 (#21), and PyrII-5 (#29). Figure 1(a) already showed the effective strain field E_{eff} , based on the displacement gradient tensor \mathbf{H}^{exp} , which is calculated by taking the gradient of the displacement field:

$$\mathbf{H}^{\text{exp}} = \vec{\nabla}_0 \vec{u} = \begin{bmatrix} H_{xx}^{\text{exp}} & H_{xy}^{\text{exp}} \\ H_{yx}^{\text{exp}} & H_{yy}^{\text{exp}} \end{bmatrix}. \quad (1)$$

The effective strain E_{eff} is a shear-dominated strain measure indicative of slip, derived from the in-plane components of \mathbf{H}^{exp} [31]:

$$E_{\text{eff}} = \sqrt{\frac{1}{2} (H_{xx}^{\text{exp}} - H_{yy}^{\text{exp}})^2 + (H_{xy}^{\text{exp}})^2}. \quad (2)$$

The slip system's contribution to the displacement gradient tensor, for a single slip system α , is expressed as the product of the slip amplitude γ^α and the Schmid tensor \mathbf{P}^α :

$$\mathbf{H}^\alpha = \gamma^\alpha \mathbf{P}^\alpha = \gamma^\alpha \vec{s}^\alpha \otimes \vec{n}^\alpha, \quad (3)$$

with \vec{s}^α and \vec{n}^α representing the normalized slip direction and slip plane normal of slip system α , respectively. When considering multiple active slip systems, the local theoretical displacement gradient tensor \mathbf{H}^{theo} is the sum of contributions from each system:

$$\mathbf{H}^{theo} = \sum_{\alpha=1}^N \mathbf{H}^{\alpha}. \quad (4)$$

The original SSLIP method [22] is predicated on the assumption that the measured in-plane displacement gradient tensor components can be described by a linear combination of Schmid tensors of active slip systems, each with a certain slip amplitude. The optimization problem, defined at every datapoint, aims to minimize the sum of the absolute values of the slip activities, while constraining the tensor residual norm $R_{2D}^{L_2}$ below a predefined threshold H_{thresh} (based on DIC noise level):

$$\underset{\gamma^{\alpha} = \gamma^1, \dots, \gamma^N}{\text{minimize}} \quad \sum_{\alpha=1}^N |\gamma^{\alpha}| \quad (5a)$$

$$\text{subject to} \quad \|\mathbf{H}^{exp} - \mathbf{H}^{theor}\|^{2D} < H_{thresh}. \quad (5b)$$

The minimization of the sum of absolute values of slip activities is included in order to handle more than 4 slip systems, since there are only 4 measured (known) components of the in-plane 2D displacement gradient tensor. In the original SSLIP paper [22], we showed that this approach works well for a less complicated HCP virtual experiment and also for FCC and BCC real experiments. However, as shown in Figure 1, application to the challenging HCP virtual experiment with 4 overlapping slip systems from different slip families results in erroneous results.

2.2. +SSLIP part I: Automated Preselection Using the Radon Transform

To increase the robustness, the +SSLIP methodology first incorporates a new step for automated preselection of slip systems through the Radon transform, as initially proposed by Hu *et al.* [13]. An important difference with the method of Hu *et al.* is that we use the Radon transform only for de-selection of slip systems that clearly cannot be active, while the actual identification is done in the second part of the +SSLIP method, as discussed below. The Radon transform projects a 2D function, in this case the measured effective strain field E_{eff} , from Cartesian coordinates (x, y) to Polar coordinates (θ_{pr}, x') [30]:

$$\mathcal{R}\{E_{eff}(x, y)\} = \iint_D E_{eff}(x, y) \delta(x' - x \cos \theta_{pr} - y \sin \theta_{pr}) dx dy. \quad (6)$$

In this, θ_{pr} denotes the projection angle and x' signifies the radial distance for the given projection angle. This projection into Radon space yields a sinogram that highlights dominant slip orientations as intensity peaks, as illustrated in Figure 2(a-c). In Figure 2(d), the identified slip traces are shown with their

corresponding angles, which agree almost perfectly with the measured ones in Figure 2(c).

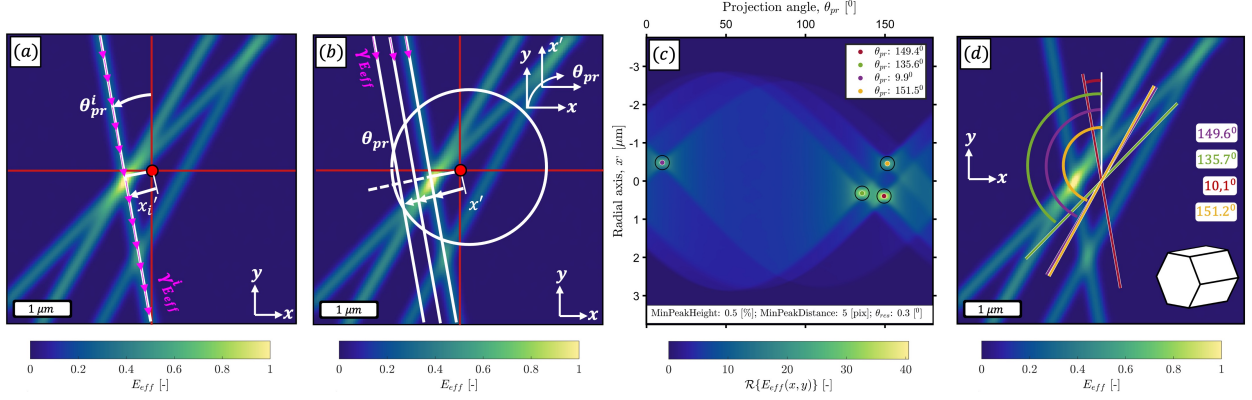


Figure 2: Application of the Radon transform to the Virtual HCP Experiment. (a) Effective strain field, E_{eff} , with superimposed lines indicating the projection angles, θ_{pr} , used in the Radon transform. The intersection point, x_i , marks the center of the local area considered for analysis. (b) The effective strain field with a circular overlay representing the Radon transform's integration path. The red dot at the center indicates the rotation axis for the Radon transform. (c) The Radon transform output, $\mathcal{R}\{E_{eff}(x, y)\}$, with peaks corresponding to prominent slip band angles in the strain field. (d) Identified slip band orientations superimposed onto the strain field, with color-coded lines representing different slip system, detected by the Radon transform, with corresponding (theoretical) angles.

While this works well on the virtual experiment, we try this now on an experimental strain field to assess its performance. Figure 3(a) shows the strain field of a grain from the dataset of the case study in Section 3. Its Radon transform, shown in Figure 3(b), shows a clear maximum as illustrated with the red ellips, which, as will be shown, does not correspond to the slip band orientations. Therefore, we address the influence of the grain shape by introducing a correction step, similarly to the approach by Hu *et al.* [13]. A binary mask of the grain shape (Figure 3(c)),

$$g(x, y) = \begin{cases} 1, & \text{for } (x, y) \text{ inside the grain} \\ 0, & \text{for } (x, y) \text{ outside the grain} \end{cases}, \quad (7)$$

is employed to normalize the Radon transform outputs. The Radon transform of this grain shape function, $\mathcal{R}\{g(x, y)\}$,

$$\mathcal{R}\{g(x, y)\} = \iint_D g(x, y) \delta(x' - x \cos \theta_{pr} - y \sin \theta_{pr}) dx dy, \quad (8)$$

is shown in Figure 3(e). The same Radon maximum values are seen as in Figure 3(d), which confirms that the slip bands are missed. Next, normalization of the peak heights in the original Radon space is performed:

$$\overline{\mathcal{R}}\{E_{eff}(x, y)\} = \frac{\mathcal{R}\{E_{eff}(x, y)\}}{\mathcal{R}\{g(x, y)\}}. \quad (9)$$

This ensures that the length of integration reflects the actual slip trace length within the grain, as shown in Figure 3(f), wherein the Radon peaks actually correspond to the slip bands. Figure 3(c) shows the strain map again with the identified (Basal) slip trace.

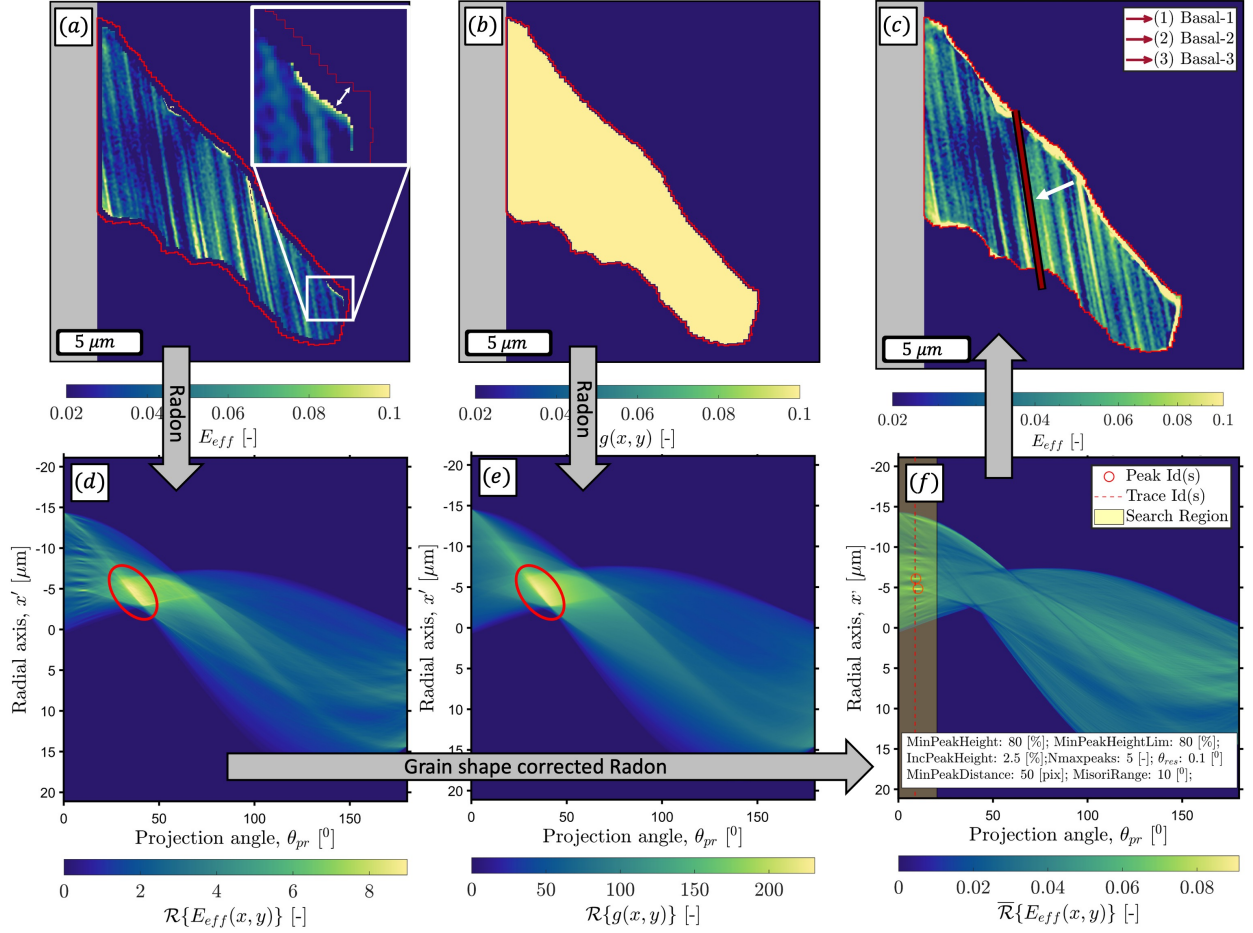


Figure 3: Experimental Grain Analysis Using Normalized Radon transform. (a) Effective strain field within a single grain, E_{eff} , with a magnified inset detailing the grain boundary. (b) Binary mask derived from the strain field to define the grain boundary for normalization. (c) Superimposed identified Basal slip trace on the strain field, conforming to the identified Radon transform peaks. (d) Raw Radon transform, $R\{E_{\text{eff}}(x, y)\}$, displaying the intensity of features as a function of the projection angle, θ_{pr} , and radial axis, highlighting the maximum values with a red ellipse. (e) Grain shape Radon transform, $R\{g(x, y)\}$, which accounts for the curvature of the grain boundary, showing a similar profile to that of (d). (f) Corrected Radon output with peak indicators and trace lines corresponding to the detected slip bands within the search region, illustrating the precision of slip band orientation identification post grain shape normalization.

This normalization process, using the grain shape function $g(x, y)$, ensures that the length of integration accurately reflects the actual length of slip traces within the grain. The normalized Radon transform, $\bar{R}\{E_{\text{eff}}(x, y)\}$, isolates the average strain along each projection line, enhancing the precision of slip system orientation identification. Peaks within the normalized sinogram, identified using the `peaks2` function in

Matlab, represent slip band orientations, thereby automating the trace analysis process and warranting the preselection efficiency and objectivity within the +SSLIP framework.

As a preliminary demonstration, we show in Figure 4 the Radon transform preselected slip systems for all experimental cases considered in this paper. The simple example grain shown in Figure 3 resulted in preselection of only a single slip family, i.e. Basal, in which case it could be argued that further identification with +SSLIP is not required, since a SF based method of, e.g., Hu et al. [13], would perform well here in the case that the slip system with the highest SF within a slip family always activated. However, especially for smaller grains with fewer dislocation sources, this assumption may be questionable. Moreover, Figure 4 shows that all other grains considered in this work show at least 3 preselected slip families (each grain showing at least 6 slip systems). Therefore, it is unreasonable in these cases to rely just on the SF for further selection, especially when the critical resolved shear stresses can be unknown, as is often the case. Additionally, while Figure 4(a,b) show clear slip bands that are visually conforming well to the preselected slip traces, the initial Radon-based preselections of the grains in Figure 4(c-e) are less conclusive. In summary, the Radon transform is a valuable first step, but the SSLIP analysis is required to achieve positive identification of the precise slip system(s).

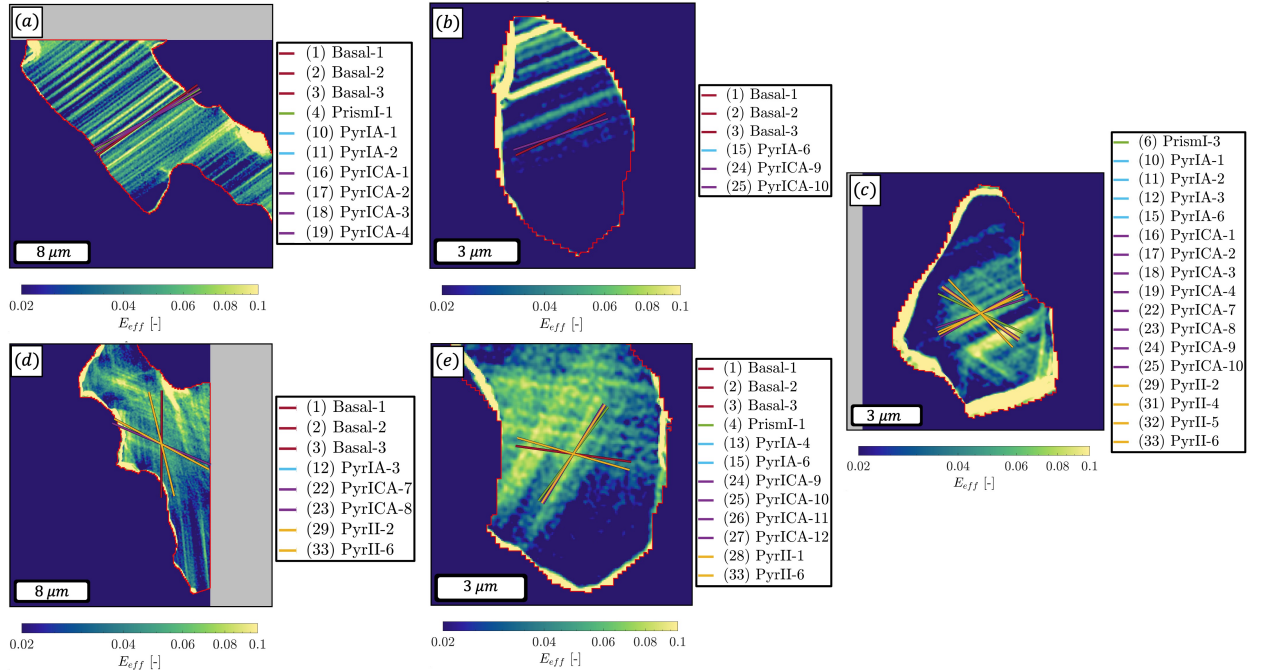


Figure 4: Demonstration of Radon transform preselection on all grains considered in this work. For each grain, (a-e), the effective strain field E_{eff} is plotted. The slip traces of the preselected slip systems are drawn as overlay, as described in the legends.

2.3. +SSLIP part II: SSLIP Analysis with Preselected Slip System Combinations

With the Radon transform providing a trace-based preselected set of slip systems, we can now apply SSLIP in a targeted manner. For improved robustness and to avoid erroneous solutions from in-plane linearly dependent slip systems, we follow a refined approach that involves systematically examining every possible combination of two slip systems from the preselected pool, at each datapoint. Essentially, this means conducting SSLIP analysis N times for every datapoint, where N represents the total number of unique two-system combinations from the preselected set:

$$N = \frac{N_{radon}!}{2! * (N_{radon} - 2)!} \quad (10)$$

For the current virtual experiment, preselection excludes 16 of the 24 slip systems, only leaving 3 Basal systems, 1 Prismatic system, 2 PyrICA systems and 2 PyrII systems to be included ($N_{radon} = 8$). Thus, according to Eq. 10, this results in $N = 28$ combinations to be analyzed by SSLIP. Below, we will detail the criteria and process for selecting the optimal combination for each datapoint, ensuring a precise and comprehensive identification of active slip systems.

2.3.1. SSLIP Analysis with Preselected Slip System Combinations

With the set of preselected slip systems established, we proceed to explain the SSLIP analysis phase. This involves evaluating every possible combination of two slip systems from the preselected pool for each datapoint within a certain grain. Specifically, for each pair of slip systems, we apply the SSLIP methodology, utilizing the optimization equation (Eq. 5). Additionally, rotation correction will be applied, as explained below in Section 2.4.

The selection of the optimal combination for each datapoint is governed by the residual fraction, $Rf_{2D}^{L_2}$, which must fall below a predefined threshold to ensure accurate identification. This residual fraction is calculated as

$$Rf_{2D}^{L_2} = \frac{\|\mathbf{H}^{exp} - \mathbf{H}^{theo}\|^{2D}}{E_{eff}}, \quad (11)$$

where \mathbf{H}^{exp} represents the experimental displacement gradient tensor, \mathbf{H}^{theo} denotes the theoretical displacement gradient tensor predicted by a combination of slip systems and rotation (see Section 2.4), and E_{eff} is the effective strain, serving as a normalization factor.

The constraints imposed on potential combinations are outlined in Table 1.

Table 1: Parameters for SSLIP Analysis Selection Criteria

Parameter	Symbol	Value	Unit
Max. Displacement Gradient Tensor Residual Fraction	$RJ_{2D}^{L_2, max}$	0.2	[-]
Min. Equivalent Strain	E_{eff}^{min}	0.02	[-]
Max. Allowable Rotation Correction	γ_{rot}^{max}	5	[$^\circ$]

Each combination is thereby assessed based on its residual fraction (Eq. 11), rotation angle and minimum equivalent strain, according to the values specified in Table 1. These values have been chosen as they were found to work robustly for the analysis of hundreds of Zn grains, of which a few challenging cases are discussed in Section 3. Among these valid combinations, the one with the lowest sum of slip amplitudes, thereby indicating the path of least resistance and conforming to the principle of minimum energy, is selected as the definitive combination of slip system activities for that particular datapoint.

2.4. +SSLIP part III: Rotation Correction in SSLIP

Since SSLIP will be applied with only two systems at a time, the optimization problem will have fewer degrees of freedom, which allows us to simultaneously identify the local elastic rotations. Inclusion of local elastic rotations was not needed earlier for the less challenging cases of FCC and BCC, but is found to be necessary for HCP because of its large number slip systems with linearly dependent in-plane deformation gradient tensor (due to the high anisotropy and wide range of slip families of HCP). In practice, these rotations can be in the form of (full) grain rotation (e.g. due to grain boundary sliding), by compatibility effects near a grain boundary or other microstructural features [4], or simply by misalignment of the sample between (quasi-situ) measurement steps. Therefore, we add (local) rotation correction to the methodology, which will not only improve the slip system identification but will also give an extra result, i.e. the rotation field, which may be useful for the analysis.

The correction involves incorporating an additional rotation component into SSLIP, represented by a simplified rotation tensor. For small rotations, which are common in our observations, the in-plane rotation tensor can be described and simplifies as follows:

$$\mathbf{H}^{rot} = \begin{bmatrix} \cos(\theta) & -\sin(\theta) \\ \sin(\theta) & \cos(\theta) \end{bmatrix} - \mathbf{I} \approx \theta \begin{bmatrix} 0 & -1 \\ 1 & 0 \end{bmatrix}. \quad (12)$$

Here, θ represents the rotation angle and, under the assumption that θ is small, $\sin(\theta) \approx \theta$ and $\cos(\theta) \approx 1$,

allowing us to capture the in-plane rotation approximately with this simplified matrix, in displacement gradient tensor form. It is then incorporated into SSLIP as an additional slip system, for each combination that will be tried. This results in the rotation value θ at every datapoint, along with the slip system activities. In cases where the rotations would be so large that the simplified rotation tensor is a poor estimate, then the full version of \mathbf{H}^{rot} in Eq. 12 can be used, at the expense that \mathbf{H}^{rot} needs to be updated using the current estimate of the rotation angle, at each location and at each step in the iterative optimization routine.

2.5. Validation on Virtual Experiment

Now, the full +SSLIP methodology is applied to the challenging HCP virtual experiment, for which the results are shown in Figure 5. This figure is structured identically to those in the experimental case study below. Figure 5(a) shows the crystallographic orientation of the virtual experiment and Figure 5(b) shows again the effective strain field. Application of the Radon transfer results in 8 preselected slip systems, see Figure 2. Subsequently, application of Rotation-corrected SSLIP on all pairs of the slip systems ($N = 28$) and point-wise selection of the pair with the lowest residual results in the slip activity fields as shown in Figure 5. The correct slip systems were Basal-3, PrismI-3, PyrICA-9 and PyrII-5, all of which show a single slip band, oriented as expected along their slip trace. The other 4 pre-selected, but non-active, slip systems show no activity over the full area, as expected. The error of the SSLIP analysis is represented by the residual norm fraction in Figure 5(d), $Rf_{2D,max}^{L2}$ (Eq. 11), in which low values can be observed. No rotation was applied in the virtual experiment, which is reproduced by the +SSLIP algorithm as shown in Figure 5(c). The intersection of 3 slip bands in the center of the domain cannot be identified, since only 2 slip systems can be active per datapoint. Importantly, these intersections are also not falsely attributed to incorrect slip systems. In practice, the slip activity at such multi-slip intersections can easily be inferred from the neighbouring slip activity. Overall, the identification shown here is robust and accurate and shows promise for identification of complex HCP activities.

2.6. Conclusive vs. nondiscriminatory identification

At this point it may seem that the +SSLIP method is working perfectly, at least on this virtual test, but one issue has been left undiscussed, i.e. the possible non-uniqueness of the 2D part of a slip system's displacement gradient tensor for specific grain orientations. In theory, even though each slip system has of course a unique 3D displacement gradient, the 2D part of the displacement gradient tensor could be exactly, or almost, the same for two (or more) slip systems, making those slip systems fundamentally nondiscriminatory in the SSLIP method. In practice, however, the minimization of the sum of slip activities,

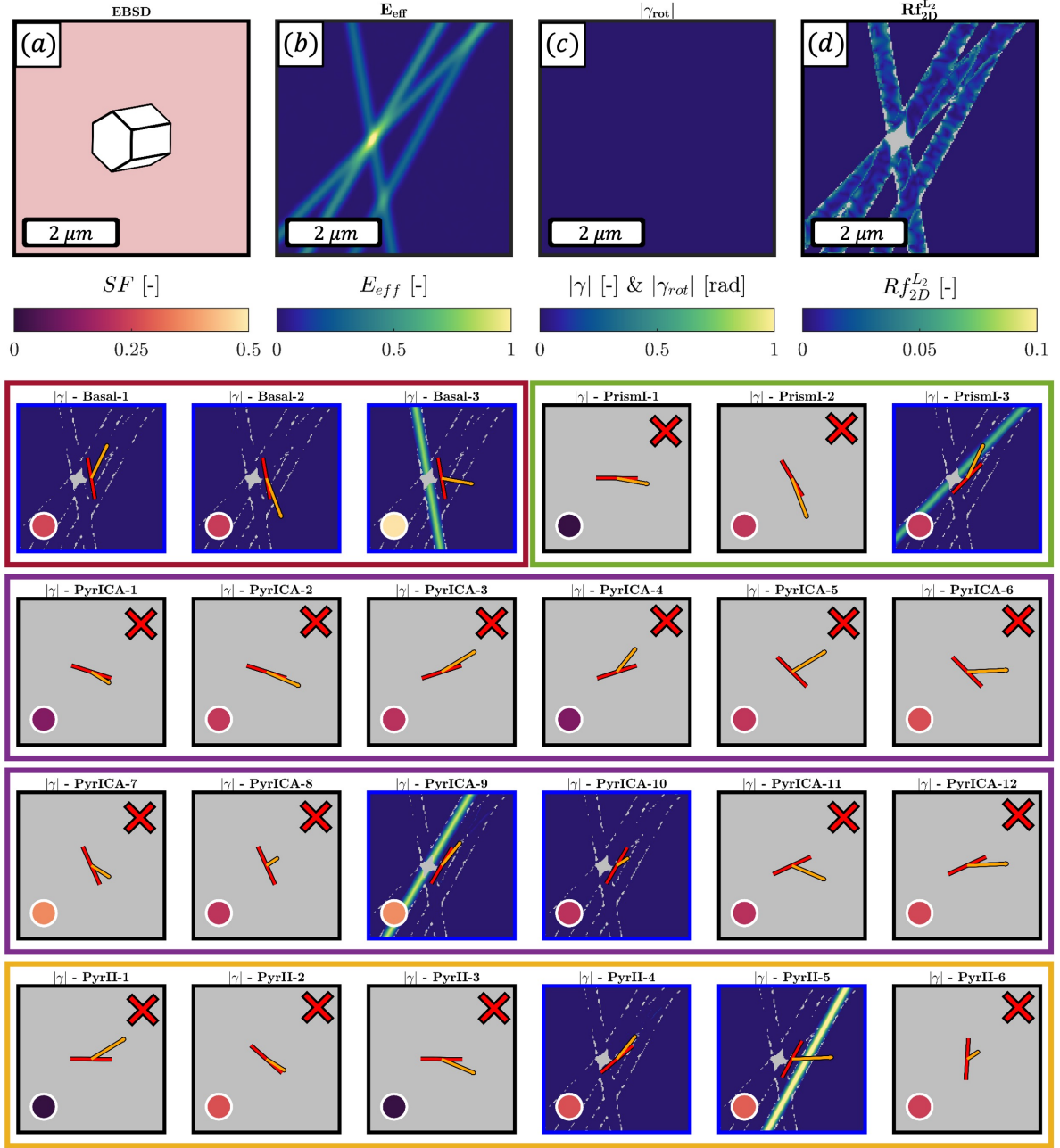


Figure 5: Demonstration of the +SSLIP results on the challenging virtual experiment. (a) The EBSD map and rotated crystal shape illustrates the crystal orientation of this virtual experiment. (b) The effective strain field, E_{eff} , showing the deformation pattern, with 4 slip bands clearly visible. (c) The rotation field, γ_{rot} , resulting from rotation-correction by +SSLIP. (d) The residual strain fraction field, Rf_{2D}^{L2} , resulting from +SSLIP, showing the fit between the "experimental" and theoretical displacement gradient tensor. Below that, the slip system activity map of each slip system of each slip family (Basal, PrismI, PyrICA and PyrII) is shown. Maps with red crosses indicate that systems were not selected by Radon transform preselection. Each map also features the slip trace (red line) and direction (orange arrow), with the Schmid factor (SF) depicted as colored circles (colorbar below (a)). The SF is not used in the +SSLIP method.

as used in the original SSLIP method [22], was found to be robust against slip systems with almost equal 2D displacement gradient tensors, therefore, this issue was not considered in detail before. For HCP, however, there are many potential slip systems from multiple different families (which typically cannot be excluded a-priori due to unknown CRSS values) and the occurrence of multiple highly similar 2D displacement gradient tensors was found to be problematic for grains with 'unfortunate' grain orientation, a few examples of which are treated in Section 3. In such cases, a group of 2 or more slip systems can be defined with similar enough 2D displacement gradient tensors such that the measured slip activity can only be assigned to the group of slip systems. When slip activity is assigned to such a 'nondiscriminatory slip system group' we call the identification 'inconclusive', as counterpart to the regular 'conclusive' identification where the slip activity is uniquely assigned to one or more slip systems.

Therefore, in the +SSLIP method, after the Radon transform preselection, all possible nondiscriminatory slip system groups are identified from the available preselected slip systems, before executing the +SSLIP identification. Whether or not the theoretical 2D displacement gradient tensor of a preselected slip systems can be discriminated from the experimentally measured 2D displacement gradient tensor caused by activity of another slip systems depends on the absolute measurement accuracy of the slip trace angle and the projected slip direction angle, which depends on the combined accuracy of EBSD, SEM-DIC (including SEM scanning artefacts), and their mutual alignment. For our case, it was found that these two angles can have an error up to $\sim 5^\circ$. Therefore, we define an angle threshold of 5° , i.e. if two preselected slip systems have both a slip trace angle and projected slip direction angle within 5° of each other, they are considered nondiscriminatory. Through this procedure, the preselected slip systems are, when necessary, included in nondiscriminatory slip system groups in the +SSLIP identification. In the (pixel-wise) +SSLIP output, the slip activity assigned to a nondiscriminatory group is attributed equally to each slip system within the group. The way this works in practice will be shown in the section below (note that the virtual test case in Figure 5 is a regular example of a 'conclusive' identification).

3. Experimental Case Study: +SSLIP applied on HCP Zinc Coating

In this section, we demonstrate the strength of the +SSLIP method on experimental SEM-DIC results of an HCP Zinc anti-corrosion coating, which will show activities from multiple slip families: Basal, PyrI and PyrII. The focus will be on challenging cases that include, .e.g., multiple 'nondiscriminatory slip system groups'. Additionally, we will showcase robust identification on grains that exhibit cross slip and diffuse slip, for which pure trace-based analysis is hardly possible [22].

In Section 3.1, we briefly detail the experimental methodology for acquiring microstructure-aligned SEM-DIC strain fields. Section 3.2 demonstrates +SSLIP a simple case of single slip and Section 3.3 shows how an inconclusive identification can be interpreted. More complex cases of multi-slip, cross slip and diffuse slip are treated in Sections 3.4 and 3.5.

3.1. Material Characterization and SEM-DIC testing

The material used in this case study is a hot-dip galvanized skin-passed Zn coated steel sample whose material code is DX54-Galvanized Iron (GI). The thickness of the Zn anti-corrosion coating is approximately 10 μm . Dogbone samples are cut using wire-EDM such that they can be deformed using a Kammrath&Weiss tensile stage mounted inside a Tescan Mira 3 SEM, at close working distance, in order to optimize the spatial resolution of SEM-DIC [5, 32]. The gauge width is 4 mm and sample thickness is 0.7 mm. Before testing, the sample surface is carefully prepared in a single step of polishing using Oxide Polishing Suspension (OPS)-NonDry and ethanol (1:1) suspension on a Struers MD-Chem cloth for 10 minutes. This short polishing provides the optimal compromise between good surface quality and low material removal, since the Zn coating is very thin.

Next, several $\sim 50 \mu\text{m}$ sized Regions of Interest (RoI's) are chosen for characterization and *in-situ* SEM-DIC testing, as shown in Figure 6 for one RoI. EBSD is performed with an EDAX Digiview 2 camera in a Tescan Mira 3 SEM, with offline spherical indexing using EMSphInx for improved quality [33], resulting in an Inverse Pole Figure (IPF) map as visualized in Figure 6(a). Subsequently, we apply a fine and dense InSn SEM-DIC speckle pattern applied according to the parameters of pattern **b** in Table 1 of Hoefnagels *et al.* [34], resulting in approximately 90-100 nm sized speckles, see Figure 6(b). The specimen is then mounted in a Kammrath&Weiss micro-tensile stage, which is installed inside the Tescan Mira 3 SEM for interrupted *in-situ* testing, at deformation steps as shown in Figure 6(d). For SEM-DIC imaging, we use in-lens SE imaging at a 5 kV beam voltage and at 7 mm working distance. At each deformation step, a horizontal and vertical scan are captured that are combined into a single image that is corrected for SEM scanning artefacts, using a software program called *ScanCorr* [4]. Subsequently, DIC is performed on these scanning artefacts corrected images using the MatchID software, employing parameters as given in Table 2, following procedures proposed by Vermeij *et al.* [4, 32]. Subsequently, the nanomechanical alignment framework [4] is applied to allow direct spatial correlation between EBSD and DIC data, as observed in the strain maps of all deformation steps in Figure 6(e), with the aligned grain boundary overlaid.

At a first glance, the materials reveals a range of deformation mechanisms. Crystallographic slip can be observed within grains, both in the form of sharp and more diffuse slip bands. Additionally, localizations

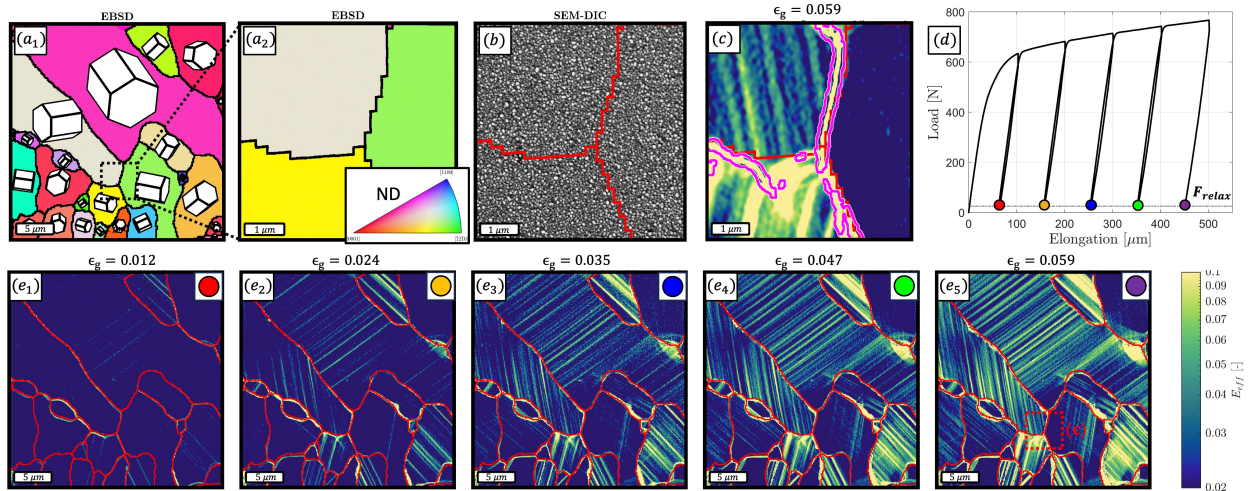


Figure 6: (a₁) Electron Backscatter Diffraction (EBSD) IPF map illustrating the microstructure of the Zn coating prior to deformation, with hexagonal shapes illustrating the crystal orientations. (a₂) Zoom-in of IPF map around a triple junction. (b) Scanning Electron Microscope (SEM) image, in in-lens Secondary Electron (SE) mode, displaying the Indium-Tin (InSn) speckle pattern used for Digital Image Correlation (DIC). The aligned grain boundaries are shown as overlay in red. (c) Effective strain field captured (inset of (e₅) via DIC at a global strain of 0.059, showing crystal slip and grain boundary deformation. Areas surrounded by pink lines denote interpolated DIC data, predominantly on grain boundary locations. (d) Load-elongation curve from the *in-situ* tensile test with color-coded points corresponding to the strain levels in subfigures (e₁)-(e₅). (e₁)-(e₅) Effective strain fields at progressive tensile test increments, highlighting the evolution of strain localization and the alignment with EBSD data.

occur on top of grain boundaries, hinting at the occurrence of grain boundary sliding and/or migration. Figure 6(c) shows this more clearly with an inset of the strain field around a triple junction, for the final deformation step. Distinct slip, diffuse intragranular deformation and grain boundary activity can be observed. Note that the grain boundary deformation is very strong and resulted in a local degradation of the DIC pattern, such that interpolation of the DIC data was required (in the areas outlined with a thin pink line) [5]. However, the grain boundary deformation is outside the scope of this paper and will be subjected to identification by an alternative variation of the SSLIP method that is focused on the identification of grain boundary sliding [35]. Here, the goal is identification of the active slip system inside (all of) the grains.

With the microstructure-correlated deformation data available, we will now demonstrate the +SSLIP method on several HCP Zn grains. For this, we choose several individual grains that show slip activity, starting with simple basal slip and moving on to multiple and differently oriented slip bands in Section 3.4. Additionally, "nondiscriminatory" slip systems will be handled transparently when encountered. In Section 3.5, we will focus on more complex cases of cross slip and diffuse slip, on which the +SSLIP method excels.

For each experimental case, we extract the deformation data of a single grain, allowed by the data

Table 2: DIC System and Correlation Parameters

Parameter	Value	Unit
Capture Instrument	Tescan Mira 3 SEM	-
Field of View	40	[μm]
Pixel Size	13	[nm]
DIC Software	MatchID	-
Correlation Algorithm	ZNSSD	-
Subset Size	33	[pix]
Step Size	3	[pix]
Matching Criterion	Zero-normalized sum of squares differences	-
Pre-filtering	Gaussian	-
Filter Size	1	[pix]
Correlation Threshold	≥ 0.7	-
Subset Shape Function	Affine	-

alignment, and remove a band of 5 pixels along the grain boundary to avoid any grain boundary sliding and/or migration mechanisms. Additionally, the peak identification on the sinograms is performed to only retrieve peaks that are above 80 % of the maximum value are identified, with a maximum of 5 peaks.

3.2. +SSLIP applied on Zn: single slip

The first experimental grain that we investigate is shown in Figure 7. An impression of the crystallography and the deformation of the grain is given in Figure 7(a-b), consisting of the EBSD map and the effective strain field. At a first glance, slip occurs over only one specific slip plane, making it a relatively simple case to start the demonstration of the +SSLIP methodology.

Application of +SSLIP results in identification of the slip activity fields as shown in Figure 7. As expected, the Radon transform preselection only picks up one specific trace, which in this case can be attributed to 6 individual slip systems: all 3 Basal systems, 1 PyrIA system and 2 PyrICA systems. Among these, Basal-2 and Basal-3 are identified as the active slip systems, which is unsurprising since Basal slip is known to have the lowest CRSS in Zn [7, 36]. The rotation field in Figure 7(c), identified by +SSLIP, shows a negligible contribution for this grain. Additionally, the residual fraction in Figure 7(d) is rather low, indicating that the identification was successful. Note that the rotation field and the residual fraction field is set to NaN (i.e. shown as grey in the figures) when the residual fraction is above its threshold or when the effective strain is below its threshold.

While this example may seem rather straightforward, the activities of the three Basal slip systems do not follow Schmid's law globally. In fact, the lowest SF Basal system, Basal-3, shows most of the activity, while the highest SF system, Basal-1, shows no activity. Likely, the local loading conditions in the polycrystalline coating change the local stress state, rendering the SF insufficient to predict slip system activities. This

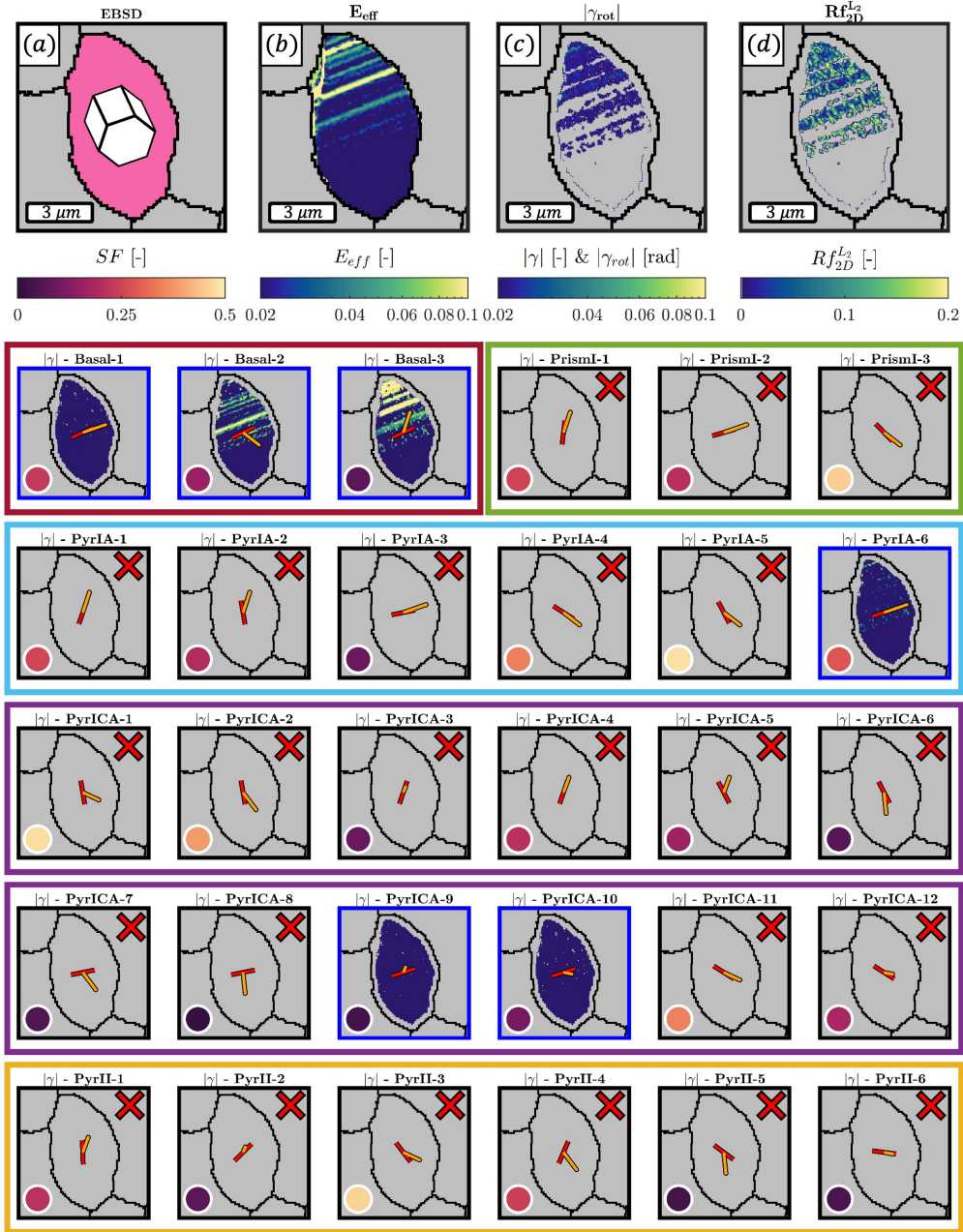


Figure 7: Results of slip system identification for a selected HCP Zn grain, showing one type of slip bands, using the +SSLIP method. (a) The EBSD map and rotated crystal shape illustrates the crystal orientation. (b) The effective strain field, E_{eff} , showing the deformation pattern. (c) The rotation field, γ_{rot} , resulting from rotation-correction by +SSLIP. (d) The residual strain fraction field, Rf_{2D}^{L2} , resulting from +SSLIP, showing the fit between the experimental and theoretical displacement gradient tensor. Below that, the slip activity map of each slip system of each slip family (Basal, Prismatic, Pyramidal A, Pyramidal C and Pyramidal II) is shown. Maps with red crosses indicate that systems were not selected by Radon transform preselection. Each map also features the slip trace (red line) and direction (orange arrow), with the Schmid factor (SF) depicted as colored circles (colorbar below (a)). Note that the SF is not used in the +SSLIP method.

example shows that it is insufficient to rely on the SF.

3.3. Conclusive vs. Inconclusive Identification

As explained in Section 2.6, the identification can be inconclusive when slip systems have equal 2D (in-plane) kinematics, of which Figure 8 shows an example. The nondiscriminatory slip system groups, based on a 5° angle threshold of the slip trace and project slip direction, are annotated by specific green symbols within the Schmid factor circles of the slip system activity fields. Note that, in general, the in-plane similarity of slip systems can be judged visually by assessing the difference between the plotted slip trace and direction. In this case, there are 3 groups of nondiscriminatory systems and slip systems PrimI-1 and PyrIA-2 are each part of two nondiscriminatory groups. The green rectangle shows that Basal-1 and PyrICA-2 are nondiscriminatory, but showing limited slip activities. The two other groups, annotated by the green "+" sign (Basal-3, PrismI-1 and PyrIA-2) and circles (PrismI-1, PyrIA-1 and PyrIA-2) are very close to each other, but different enough to be separated into two groups. These two groups have the largest slip activities and it is likely that only Basal-3 is actually active, since it has a significant SF and low CRSS. Finally, this grain still has several unique slip systems, of which Basal-2 shows limited activity.

Another notable feature in this grain is the presence of rotation over almost the full grain, as shown in Figure 8(c). Considering that the magnitude of rotation (in radians) is similar to that of the slip magnitudes, SSLIP would fail here without including the rotation-correction into the identification. The resulting rotation field is almost fully smooth, which one would expect for elastic rotation, and its presence over the full grain is a strong indication of grain rotation, which may be related to grain boundary sliding.

3.4. Non-Basal multi-slip activity in Zn

After these first two examples with a single dominant slip trace in the strain map, we now turn to a more complex scenario where multiple slip systems with different trace orientations are simultaneously active. The Zinc grain analyzed in Figure 9 illustrates a case where several slip systems are active. The deformation pattern captured in the effective strain field (Figure 9(b)) reveals distinct arrays of slip bands, indicating the multi-slip nature of the deformation.

The +SSLIP method is applied here, including no less than 17 slip systems after Radon transform preselection. While this number is significant, there is only 1 group of 3 nondiscriminatory slip systems: PyrICA-2, PyrICA-7 and PyrII-2. Notably, the Basal slip systems are not among those preselected.

The +SSLIP results shown in Figure 9 clarify which slip systems are active. Slip system PyrII-2 is conclusively identified and the configuration of its activity conforms to the slip trace, which serves as an

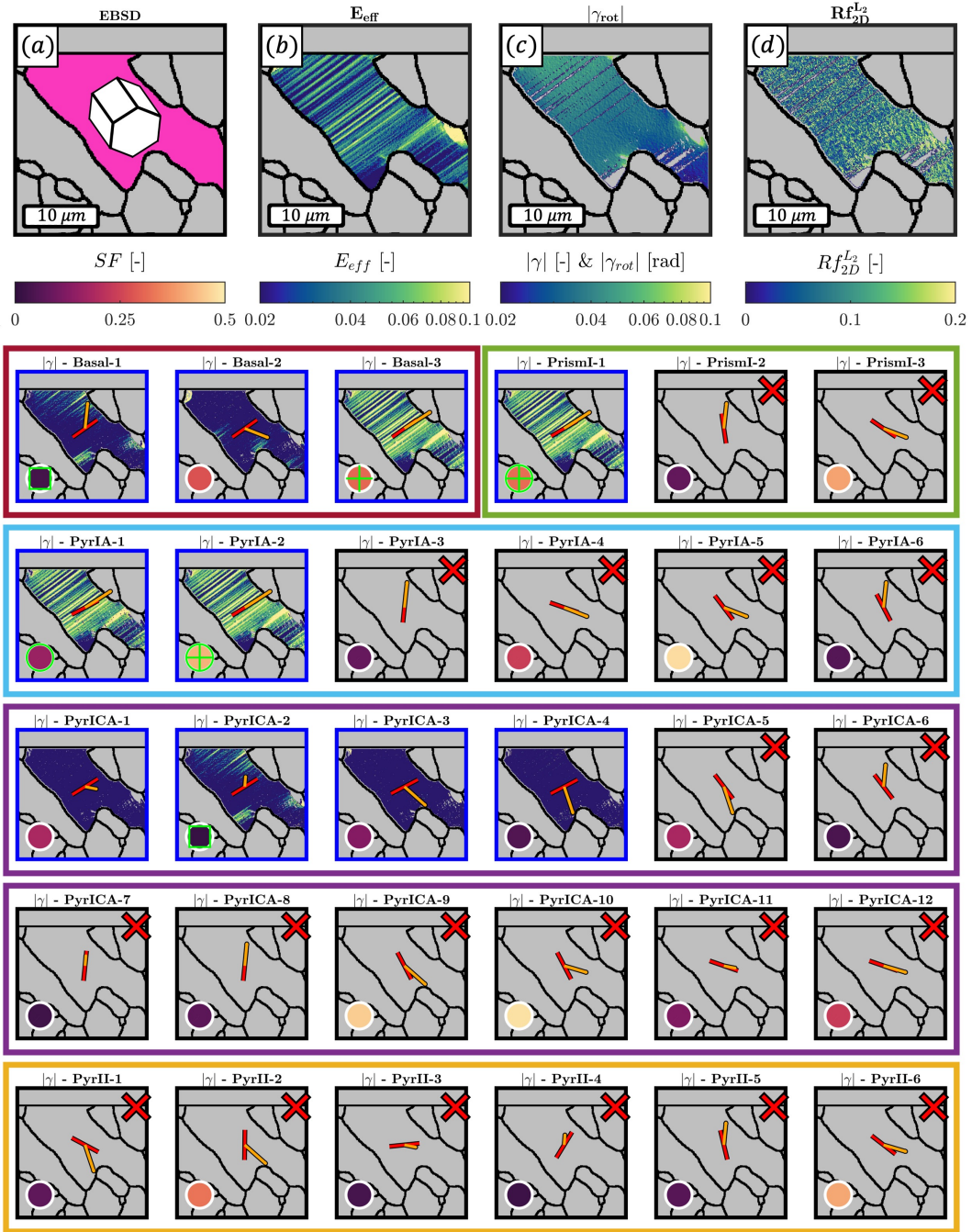


Figure 8: Evaluation of slip system activities in an HCP Zn grain using the +SSLIP method, with a focus on nondiscriminatory slip systems. The EBSD map indicates the crystal orientation (a), with corresponding effective strain (b) and rotation fields (c) illustrating the deformation. The residual fraction field (d) demonstrates the method's fit. Nondiscriminatory slip system groups are identified and marked with specific green symbols within the SF circles to denote their indistinguishability due to close angular proximity. Slip systems not preselected by the Radon transform are marked with red crosses.

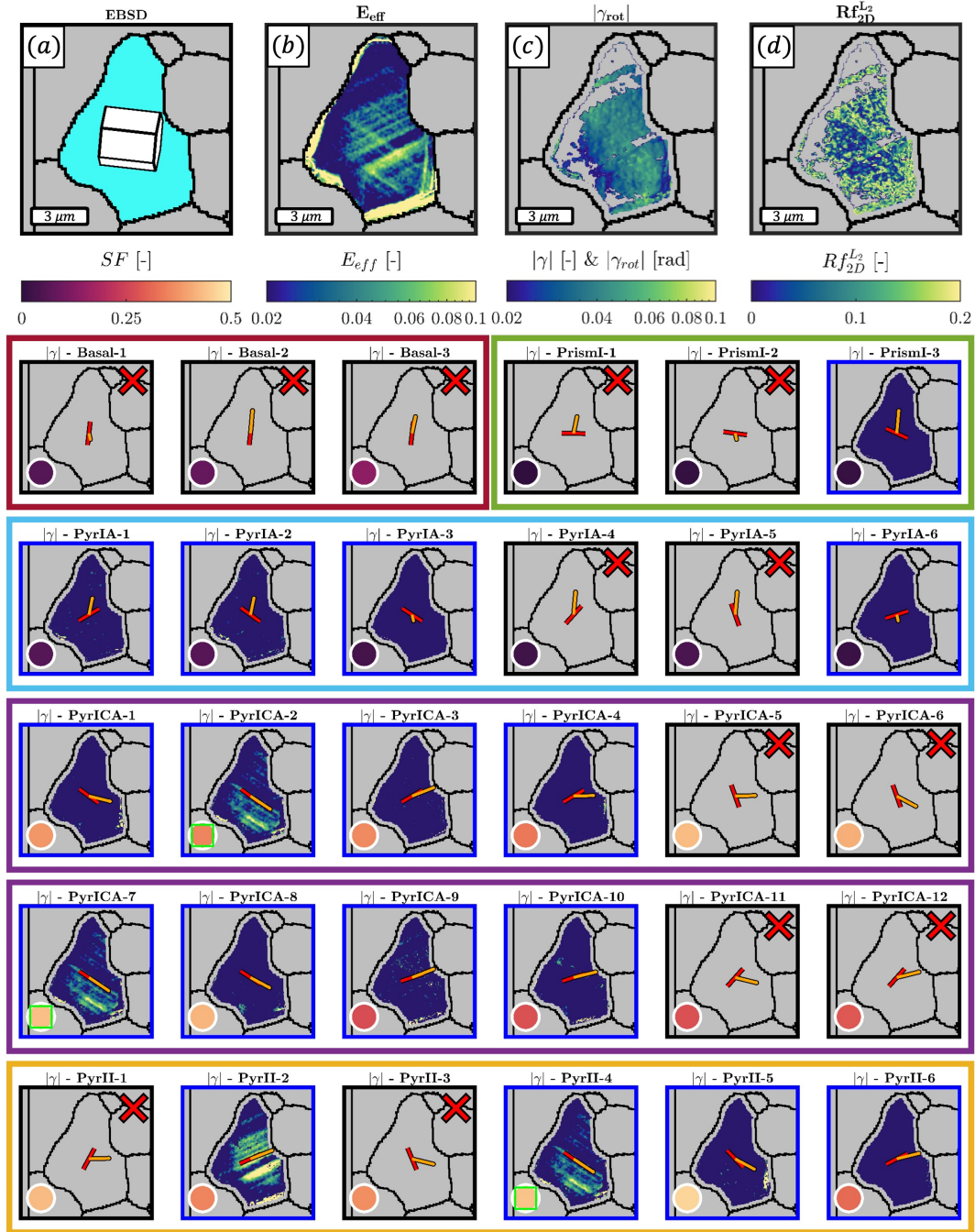


Figure 9: Complex slip system interaction in a hexagonal close-packed Zinc grain analyzed by the +SSLIP method. (a) The EBSD map indicates the crystallographic orientation of the grain. (b) The effective strain field (E_{eff}) reveals the pattern of deformation. (c) The rotation field (γ_{rot}) captures any rotations within the grain. (d) The residual strain fraction field (Rf_{2D}^{L2}) quantifies the fit quality between experimental and theoretical predictions. Below are the individual slip activity maps for each slip family, where red crosses indicate non-preselected systems.

indirect validation of the results. The other part of the deformation is attributed to the nondiscriminatory group mentioned above, for which also the traces match the observed slip system activity field. Based on this, we can conclude that Pyramidal-II can occur in this Zn alloy, with potential activity also from Pyramidal-I CA. Additionally, it shows that +SSLIP can handle a large number of potentially active slip systems.

3.5. Complex diffuse slip identified in Zn

Now, we will push the limits of +SSLIP to identify plasticity in which slip traces are not trivially identified, predominantly because the slip is diffuse and spread out over the grain. While the original SSLIP method [22] performed exceptionally well in such cases (i.e. for FCC and BCC), the added preselection by the Radon transform for +SSLIP could very well prevent such a good performance here. Therefore, we evaluate the identification on two grains which show such complexity and diffuseness.

The grain depicted in Figure 10 shows a complex deformation pattern, consisting of several sharp slip bands mixed with diffuse slip (Figure 10(b)). +SSLIP resolves 8 potential slip systems, all discriminatory, of which 3 systems show prominent slip activity. The activation of Basal-1 and particularly Basal-2 were expected due to their high SF and low CRSS, while the (near) absence of Basal-3 slip seems logical as it has the lowest SF of the three Basal systems. However, the Basal slip bands are less discrete and straight as compared to Figure 7 and Figure 8. Additionally, PyrIA-3, which has a low SF (as is the case for all of the preselected non-Basal slip systems), shows high activity, while also having considerable overlap with Basal-1.

The occurrence of PyrIA is surprising, since it has never been observed in Zn, to the best of our knowledge. This may be due to its diffuse nature, which makes it harder to identify using traditional slip trace identification methods. Interestingly, Basal-1 and PyrIA-3 have the same $\langle a \rangle$ slip direction, which provides a strong indication that cross slip is active. Cross slip allows non-planar movement in which a dislocation can move from one slip plane to another, sharing the same slip direction. It has been identified before in the original SSLIP paper in FCC and BCC [22].

Finally, we assess a grain with the highest level of complexity: a highly diffuse multi-slip deformation pattern in combination with a high number of Radon transform preselected slip systems, of which many are also nondiscriminatory, as depicted in Figure 11. Here +SSLIP considers 12 preselected slip systems, of which 5 are in a single nondiscriminatory group. Basal slip, with low SF, is conclusively identified. The differently oriented slip band activities are attributed to the nondiscriminatory group, which consists of PyrIA, PyrICA and PyrII slip systems. Notably, all slip activity fields show slip bands that concur with

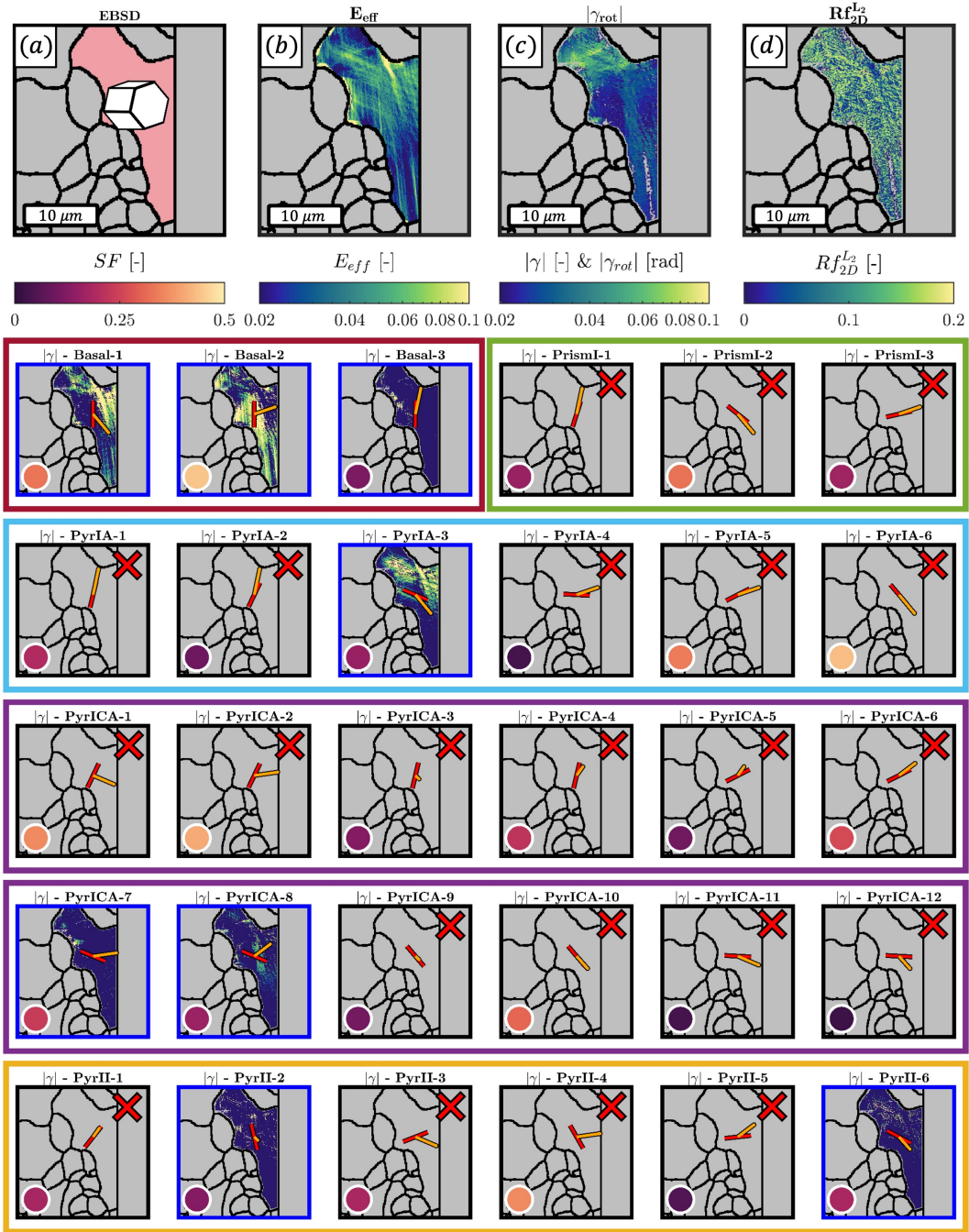


Figure 10: Diffuse and complex plasticity, potentially cross slip, identified by +SSLIP . (a) The EBSD map indicates the crystallographic orientation of the grain. (b) The effective strain field (E_{eff}) reveals the pattern of deformation. (c) The rotation field (γ_{rot}) captures any rotations within the grain. (d) The residual strain fraction field (Rf_{2D}^{L2}) quantifies the fit quality between experimental and theoretical predictions. Below are the individual slip activity maps for each slip family, where red crosses indicate non-preselected systems.

their respective slip trace orientations, agains serving as an indirect validation. The diffuse deformation pattern is thereby appropriately unraveled, even for this highly complex case.

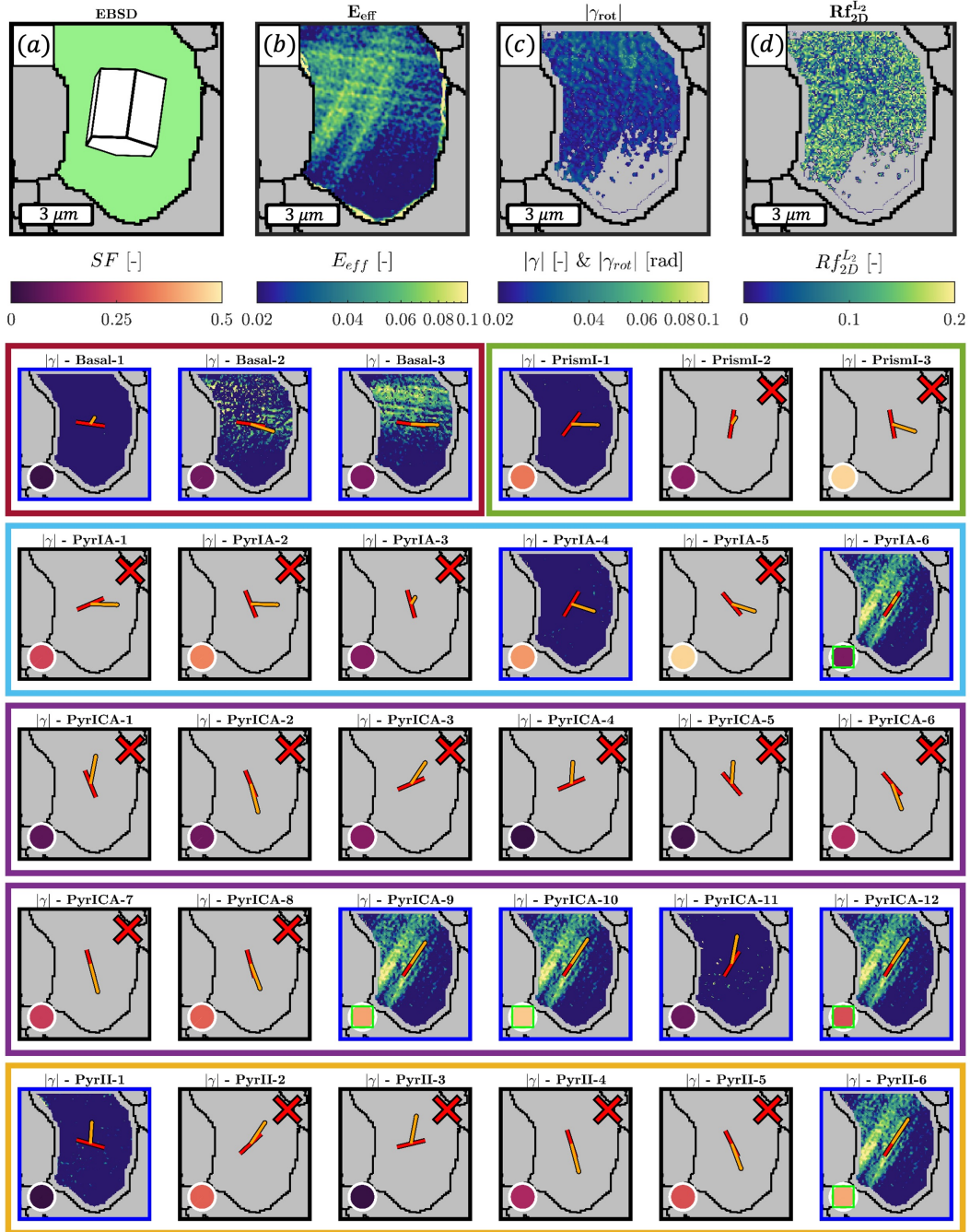


Figure 11: Diffuse crystal plasticity identified by +SSLIP . (a) The EBSD map indicates the crystallographic orientation of the grain. (b) The effective strain field (E_{eff}) reveals the pattern of deformation. (c) The rotation field (γ_{rot}) captures any rotations within the grain. (d) The residual strain fraction field (Rf_{2D}^{L2}) quantifies the fit quality between experimental and theoretical predictions. Below are the individual slip activity maps for each slip family, where red crosses indicate non-preselected systems.

4. Conclusions

In this work, we have proposed a significant extension of the original SSLIP (Slip System based Local Identification of Plasticity) method, termed as +SSLIP, addressing automated slip system identification in complex HCP metals, based on SEM-DIC and EBSD data. We have demonstrated that this methodology can effectively tackle the challenges posed by anisotropic HCP crystal structures, where the presence of multiple slip families and the resulting high number of in-plane linearly dependent slip system kinematics can complicate the analysis.

Key advancements introduced in this work include (i) automated preselection of slip systems using the Radon transform, (ii) identification of the two best matching slip systems for each data point, (iii) the incorporation of a robust rotation correction mechanism and (iv) a procedure to deal with slip systems with in-plane displacement gradient tensors that cannot be discriminated with the measurement error. This has allowed for a more precise and comprehensive identification of active slip systems, yielding the full slip system activity maps with all slip systems for each grain.

The performance of +SSLIP is first demonstrated successfully on a challenging virtual HCP case study on which the original SSLIP method did not perform well. Subsequently, we consider microstructure-correlated SEM-DIC deformation maps on a polycrystalline Zn anti-corrosion coating as an experimental case study, from which we have analyzed a number of challenging grains as proof of principle. It was found that +SSLIP overcomes the limitations of traditional trace-based analysis, particularly in cases where slip is diffuse or cross slip and diffuse slip are present. Additionally, where necessary, we provide a transparent overview of nondiscriminatory slip systems, which are fundamentally indistinguishable from only 2D (in-plane) deformation maps.

The +SSLIP approach has been confirmed to be an objective method that does not rely on factors such as the Schmid factor to select active slip systems. Indeed, every identified slip activity field shown in this paper can be indirectly validated by comparing its deformation pattern to the slip plane trace. +SSLIP offer a strong compromise between the original SSLIP method, in which preselection is not required, and SF based methods which suffer especially for HCP metals, since the critical resolved shear stress values of slip families are often unknown, while additionally the effect of neighbouring grains in a polycrystalline microstructure make the SF estimate unreliable.

In summary, the +SSLIP framework, of which the code is shared openly, stands as a significant contribution to the field of identification of plasticity, offering a robust tool for investigating and understanding the plastic deformation behavior of HCP materials. The methodology paves the way for future studies to

further explore and quantify the slip system activities under different loading conditions and in other HCP materials, which allows statistical studies and enhances the predictive capabilities of material models and simulations.

Acknowledgements

We acknowledge Marc van Maris and Mark Vissers for experimental support.

This research was carried out as part of the “Next-Coat” project, under project number N19016b in the framework of the Partnership Program of the Materials innovation institute M2i (www.m2i.nl) and the Netherlands Organization for Scientific Research (<http://www.nwo.nl>).

Code and Data availability

The Matlab code for the original SSLIP method, with several examples, is available on Github: <https://www.github.com/TijmenVermeij/SSLIP>. The +SSLIP code will be added to this repository upon acceptance of the paper. The full datasets are available upon request.

References

- [1] D. Lunt, X. Xu, T. Busolo, J. Quinta da Fonseca, and M. Preuss. Quantification of strain localisation in a bimodal two-phase titanium alloy. *Scripta Materialia*, 145:45–49, 2018.
- [2] A. Githens, S. Ganesan, Z. Chen, J. Allison, V. Sundararaghavan, and S. Daly. Characterizing microscale deformation mechanisms and macroscopic tensile properties of a high strength magnesium rare-earth alloy: A combined experimental and crystal plasticity approach. *Acta Materialia*, 186:77–94, 2020.
- [3] A. Harte, M. Atkinson, A. Smith, C. Drouven, S. Zaeferrer, J. Quinta da Fonseca, and M. Preuss. The effect of solid solution and gamma prime on the deformation modes in Ni-based superalloys. *Acta Materialia*, 194:257–275, 2020.
- [4] T. Vermeij, J.A.C. Verstijnen, T.J.J. Ramirez y Cantador, B. Blaysat, J. Neggers, and J.P.M. Hoefnagels. A nanomechanical testing framework yielding front&rear-sided, high-resolution, microstructure-correlated SEM-DIC strain fields. *Experimental Mechanics*, 62:1625–1646, 2022.
- [5] T. Vermeij, C.J.A. Mornout, V. Rezazadeh, and J.P.M. Hoefnagels. Martensite plasticity and damage competition in dual-phase steel: A micromechanical experimental-numerical study. *Acta Materialia*, 254:119020, 2023.
- [6] T. Vermeij, J. Wijnen, R.H.J. Peerlings, M.G.D. Geers, and J.P.M. Hoefnagels. A quasi-2d integrated experimental-numerical approach to high-fidelity mechanical analysis of metallic microstructures. *Acta Materialia*, 264:119551, 2024.
- [7] Rodolphe Parisot, Samuel Forest, André Pineau, Franck Nguyen, Xavier Demonet, and Jean Michel Maigne. Deformation and damage mechanisms of zinc coatings on hot-dip galvanized steel sheets: Part II. Damage modes. *Metallurgical and Materials Transactions A* 2004 35:3, 35(3):813–823, 2004.

- [8] F. Bridier, P. Villechaise, and J. Mendez. Analysis of the different slip systems activated by tension in a α/β titanium alloy in relation with local crystallographic orientation. *Acta Materialia*, 53(3):555–567, 2005.
- [9] T.R. Bieler, P. Eisenlohr, F. Roters, D. Kumar, D.E. Mason, M.A. Crimp, and D. Raabe. The role of heterogeneous deformation on damage nucleation at grain boundaries in single phase metals. *International Journal of Plasticity*, 25(9):1655–1683, 2009.
- [10] M.P. Echlin, J.C. Stinville, V.M. Miller, W.C. Lenthe, and T.M. Pollock. Incipient slip and long range plastic strain localization in microtextured Ti-6Al-4V titanium. *Acta Materialia*, 114:164–175, 2016.
- [11] A. Orozco-Caballero, D. Lunt, J.D. Robson, and J. Quinta da Fonseca. How magnesium accommodates local deformation incompatibility: A high-resolution digital image correlation study. *Acta Materialia*, 133:367–379, 2017.
- [12] M.E. Harr, S. Daly, and A.L. Pilchak. The effect of temperature on slip in microtextured Ti-6Al-2Sn-4Zr-2Mo under dwell fatigue. *International Journal of Fatigue*, 147:106173, 2021.
- [13] Haoyu Hu, Fabien Briffod, Takayuki Shiraiwa, and Manabu Enoki. Automated slip system identification and strain analysis framework using high-resolution digital image correlation data: Application to a bimodal Ti-6Al-4V alloy. *International Journal of Plasticity*, 166:103618, 7 2023.
- [14] R. Sperry, A. Harte, J. Quinta da Fonseca, E.R. Homer, R.H. Wagoner, and D.T. Fullwood. Slip band characteristics in the presence of grain boundaries in nickel-based superalloy. *Acta Materialia*, 193:229–238, 2020.
- [15] Z. Chen and S.H. Daly. Active slip system identification in polycrystalline metals by Digital Image Correlation (DIC). *Experimental Mechanics*, 57(1):115–127, 2016.
- [16] F. Bourdin, J.C. Stinville, M.P. Echlin, P.G. Callahan, W.C. Lenthe, C.J. Torbet, D. Texier, F. Bridier, J. Cormier, P. Villechaise, T.M. Pollock, and V. Valle. Measurements of plastic localization by heaviside-digital image correlation. *Acta Materialia*, 157:307 – 325, 2018.
- [17] X. Xu, D. Lunt, R. Thomas, R. Prasath Babu, A. Harte, M. Atkinson, J. Quinta da Fonseca, and M. Preuss. Identification of active slip mode in a hexagonal material by correlative scanning electron microscopy. *Acta Materialia*, 175:376 – 393, 2019.
- [18] J.C. Stinville, P.G. Callahan, M.A. Charpagne, M.P. Echlin, V. Valle, and T.M. Pollock. Direct measurements of slip irreversibility in a nickel-based superalloy using high resolution digital image correlation. *Acta Materialia*, 186:172 – 189, 2020.
- [19] R. Sperry, S. Han, Z. Chen, S.H. Daly, M.A. Crimp, and D.T. Fullwood. Comparison of EBSD, DIC, AFM, and ECCI for active slip system identification in deformed Ti-7Al. *Materials Characterization*, 173:110941, 2021.
- [20] B. Poole, A. Marsh, D. Lunt, C. Hardie, M. Gorley, C. Hamelin, and A. Harte. High-resolution strain mapping in a thermionic lab6 scanning electron microscope. *Strain*, 2024.
- [21] R.L. Black, D. Anjaria, J. Genée, V. Valle, and J.C. Stinville. Micro-strain and cyclic slip accumulation in a polycrystalline nickel-based superalloy. *Acta Materialia*, 266:119657, 2024.
- [22] T. Vermeij, R.H.J. Peerlings, M.G.D. Geers, and J.P.M. Hoefnagels. Automated Identification of Slip System Activity Fields from Digital Image Correlation Data. *Acta Materialia*, 243:118502, 1 2022.
- [23] J.C. Stinville, M.A. Charpagne, R. Maaß, H. Proudhon, W. Ludwig, P.G. Callahan, F. Wang, I.J. Beyerlein, M.P. Echlin, and T.M. Pollock. Insights into Plastic Localization by Crystallographic Slip from Emerging Experimental and Numerical Approaches. *Annual Review of Materials Research*, 53:275–317, 2023.
- [24] J. Wijnen, T. Vermeij, J.P.M. Hoefnagels, M.G.D. Geers, and R.H.J. Peerlings. High-resolution numerical-experimental

- comparison of heterogeneous slip activity in quasi-2d ferrite sheets. *arXiv preprint arXiv:2402.16199*, 2024.
- [25] J. Scherer, J. Hure, R. Madec, F. Le Bourdais, L. van Brutzel, S. Sao-Joao, G. Kermouche, J. Besson, and B. Tanguy. Tensile and micro-compression behaviour of AISI 316L austenitic stainless steel single crystals at 20 ° C and 300 ° C: experiments, modeling and simulation. *Materials Science and Engineering: A*, page 146471, 2024.
- [26] D. Agius, D. Cram, C. Hutchinson, M. Preuss, Z. Sterjovski, and C. Wallbrink. An experimental and computational study into strain localisation in beta-annealed Ti-6Al-4V. *Procedia Structural Integrity*, 45:4–11, 2023.
- [27] D. Depriester, J.P. Goulmy, and L. Barrallier. Crystal plasticity simulations of in situ tensile tests: A two-step inverse method for identification of cp parameters, and assessment of cpem capabilities. *International Journal of Plasticity*, 168:103695, 2023.
- [28] W. Yin, F. Briffod, H. Hu, T. Shiraiwa, and M. Enoki. Three-dimensional configuration of crystal plasticity in stainless steel assessed by high resolution digital image correlation and confocal microscopy. *International Journal of Plasticity*, 170:103762, 2023.
- [29] D. Konig, T. Vermeij, F. Maresca, and J.P.M. Hoefnagels. The transition of nanoscale plasticity from single- to bicrystal tensile tests extracted from a Zinc coating (working title). *In Preparation*, 2024.
- [30] S. Helgason. *The radon transform*, volume 2. Springer, 1999.
- [31] P. Paupler. *G. E. Dieter. Mechanical Metallurgy. 3rd ed., Mc Graw-Hill Book Co., New York 1986. XXIII + 751 p., DM 138.50, ISBN 0-07-016893-8*, volume 23. 1988.
- [32] T. Vermeij and J.P.M. Hoefnagels. Plasticity, localization, and damage in ferritic-pearlitic steel studied by nanoscale digital image correlation. *Scripta Materialia*, 208, 2021.
- [33] W.C. Lenthe, S. Singh, and M. De Graef. A spherical harmonic transform approach to the indexing of electron back-scattered diffraction patterns. *Ultramicroscopy*, 207:112841, 2019.
- [34] J.P.M. Hoefnagels, M.P.F.H.L. van Maris, and T. Vermeij. One-step deposition of nano-to-micron-scalable, high-quality digital image correlation patterns for high-strain in-situ multi-microscopy testing. *Strain*, 55(6):e12330, 2019. e12330 STRAIN-1507.R1.
- [35] C.J.A. Mornout, G. Slokker, T. Vermeij, D. Konig, and J.P.M. Hoefnagels. Automated identification of grain boundary sliding from digital image correlation data (working title). *In Preparation*, 2024.
- [36] W. Bednarczyk, M. Watroba, M. Jain, K. Mech, P. Bazarnik, P. Bała, J. Michler, and K. Wiecezrak. Determination of critical resolved shear stresses associated with a slips in pure Zn and Zn-Ag alloys via micro-pillar compression. *Materials & Design*, 229:111897, 2023.